Granular collapse in a fluid: Different flow regimes for an initially dense-packing

Alexis Bougouin[*] and Laurent Lacaze[†]

Institut de Mécanique des Fluides de Toulouse (IMFT), Université de Toulouse, CNRS, Toulouse, France

Laboratory experiments of the granular collapse of an initially dense-packing column in a fluid are reported. By extracting the temporal evolution of the granular material height profile, both the dynamics of the granular flow and the final deposit are characterized depending on the Stokes number St, based on a dissipative process at the grain scale, the grain-fluid density ratio r, and the aspect ratio a of the initial column. A full description of the granular collapse including the transient dynamics of the flow and the characterization of the final shape deposit is proposed. The main contribution of the present study is to provide (i) the St dependence on the granular collapse beyond the effect of the aspect ratio a already reported in previous studies, (ii) the characterization of granular flow regimes in the $((d/H_i)^{1/2}\mathrm{St}, (d/H_i)^{1/2}r)$ plane, where d/H_i is the particle diameter to initial column height ratio, and (iii) simple correlations to describe the granular collapse which would be of interest for geophysical purposes.

I. INTRODUCTION

The prevention of dramatic events involving granular materials remains a challenging task which is mostly limited by the lack of a general predictive theory for granular flows. In order to progress on the latter issue, canonical configurations dealing with the situation of dense granular flows have been extensively studied using laboratory experiments, numerical simulations, and theoretical descriptions [1]. One such configuration, which accounts for the unsteady nature of debris flows in geophysical applications, is the slumping of a granular column, initially at rest in a reservoir, on a horizontal or inclined bottom plane and often referred to as granular collapse (see Fig. 1). The case of a dry granular flow, i.e., for which the surrounding fluid can be disregarded, typically heavy coarse grains in air, has been mostly addressed in the literature. Yet many gravity-driven flows encountered in geophysical situations, such as mudflows, submarine avalanches, or landslides, are concerned with dense granular flows for which the surrounding fluid can affect the dynamics [2]. Even if generic configurations of granular-fluid flows have already been addressed in several studies [3–8], the characterization of these flows remains a challenging issue which can mainly be attributed to the large variety of phenomena observed in these situations.

The case of a dry granular collapse has been extensively studied in the literature for both axisymmetric [9,10] and quasi-two-dimensional (quasi-2D) [11–13] geometries. Both configurations were shown to lead to similar features. In the quasi-2D case, the initial granular column is characterized by its initial height H_i and the horizontal length of the reservoir L_i (see Fig. 1). When the granular medium is suddenly released on a horizontal plane, it spreads rapidly before forming a deposit characterized by a final spreading length L_f and a final height H_f located at the

*alexis.bougouin@imft.fr
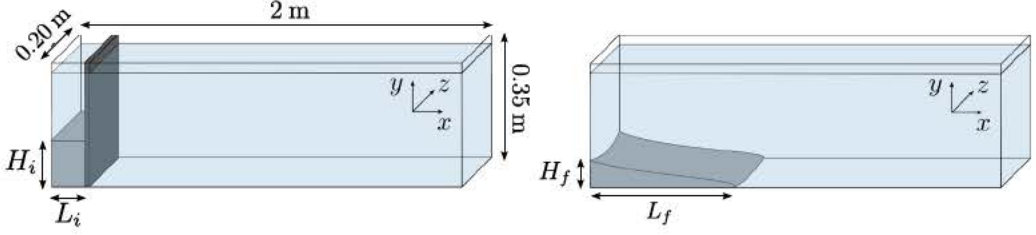†Corresponding author: laurent.lacaze@imft.fr

FIG. 1. Sketch of the experimental setup for the initial condition (granular column maintained by a vertical gate) and the final state (granular deposit).

back wall of the reservoir. All observations on dry granular collapses show that these final deposit length scales, considering an appropriate nondimensionalization, depend mostly on the initial aspect ratio $a = H_i/L_i$. In particular, the dimensionless runout $l = (L_f - L_i)/L_i$ and height $h = H_f/H_i$ were shown to have a power-law dependence on a such as

$$l \sim \begin{cases} a & \text{for } a < a_{lc} \\ a^\alpha & \text{for } a > a_{lc}, \end{cases} \tag{1}$$

$$h \sim \begin{cases} 1 & \text{for } a < a_{hc} \\ a^\beta & \text{for } a > a_{hc}, \end{cases} \tag{2}$$

where $\alpha \sim 0.7 \pm 0.1$ and $\beta \sim -0.6 \pm 0.1$ are the exponents at large aspect ratio, $a_{lc} \sim 3 \pm 1$, and $a_{hc} \sim 0.8 \pm 0.2$ [11–19]. Note that no formal model has yet been proposed to explain the values of α and β. Also, prefactors of these scaling laws are more difficult to quantify as they strongly depend on the local interaction between grains, such as the nature of the granular material [12,17] or the pore fluid pressure in the system [20].

The case of a dense granular collapse influenced by a surrounding fluid has received less attention. Thompson and Huppert [5] found that the surrounding fluid did not influence significantly the final runout and height compared to the dry case, even if the transient dynamics could highlight some different features. Yet numerical simulations have shown that the runout length, while keeping a power-law dependence on a, can be two times shorter in a viscous-dominant case than in the dry case [8]. Moreover, the initial volume fraction of the granular column has been shown to play a major role in both the dynamics of the granular flow and the shape of the final deposit, while it did not affect significantly the final shape of the deposit for the dry case [7,21]. Then, in the case of a viscous-dominant immersed granular collapse, an initial loose-packing fraction highlights the rapid dynamics and long spread of the granular mass while an initial dense-packing fraction leads to a slow dynamics and a smaller final runout length. This phenomenon has been attributed to a pore pressure feedback on the granular flow at least at the early stages of the collapse [6,22]. It is therefore strongly linked to the viscosity of the surrounding fluid and the permeability of the granular medium. It can be noted that the influence of positive pore fluid pressure in the case of a low-density and low-viscosity interstitial fluid has also been reported in the literature through laboratory experiments [20,23]. In this case, the pore pressure is controlled by fluidizing the initial granular column. The dynamics of the propagating media as well as the characteristics of the final deposit were also shown to be different from the dry granular collapse, in particular, with an enhancement of the spreading length. The role of the surrounding fluid in the granular collapse, and more particularly the transition from viscous-dominated flow to a dry configuration, remains uncertain and still deserves experimental investigation.

In order to distinguish the collapse configurations mentioned above and to qualify the transition from a viscous to a dry configuration, the granular-fluid flow can be decomposed in three different regimes (free-fall, viscous, and inertial) according to the definition of Courrech du Pont *et al.* [3]. In the case of a rotating-drum configuration, these regimes were shown to depend on two

dimensionless numbers, the Stokes number St and the grain-fluid density ratio r. The definitions of these dimensionless numbers are usually based on different ratios of timescales obtained from the dynamics of a single grain submitted to a driving force F and a drag force F_D, which is opposed to the grain motion [3,4]. In this way, the conservation of momentum on a single grain may be written

$$\frac{\pi}{6}\rho_p d^3 \frac{dv_p}{dt} = F - F_D, \tag{3}$$

where ρ_p is the density, d is the diameter, and v_p is the velocity of the particle. Different choices for these forces can be found in the literature depending on the direction along which Eq. (3) is considered, either the main flow direction or the compression direction, the latter being mostly perpendicular to the first one for avalanche configurations [3,4]. In any case, the key idea is somehow similar. In particular, F_D is defined to be either a viscous or an inertial drag force depending on the flow regime. Three different timescales can then be defined: a viscous (inertial) timescale τ_v (τ_i) that a particle needs to reach its viscous (inertial) limit velocity and a free-fall timescale τ_{ff} that a particle would need to travel prior the following solid collision when drag can be neglected. The dimensionless numbers are then defined as St $= \tau_v/\tau_{ff}$ and $r = \tau_i/\tau_{ff}$ for the Stokes number and the grain-fluid density ratio, respectively. Following Courrech du Pont *et al.* [3], one defines the distance between consecutive solid contacts in a dense granular flow as the grain diameter d, the viscous drag force as $F_D = 3\pi\mu_f d v_p$, and the inertial drag force as $F_D = (\pi/8)C_D\rho_f d^2 v_p^2$, where ρ_f and μ_f are the density and the dynamic viscosity of the ambient fluid, respectively, and C_D is a constant drag coefficient in the inertial regime. One therefore obtains

$$\text{St} = \frac{1}{18\mu_f}\left(\frac{3\rho_p F}{\pi}\right)^{1/2}, \quad r = \left(\frac{4\rho_p}{3C_D\rho_f}\right)^{1/2}. \tag{4}$$

We assume that individual grains are driven by their own weight along the slope of an avalanche during the collapse. As this slope varies along the flow, we write the associated driving force along the maximum slope which is the vertical axis (y axis in Fig. 1) as $F = (\pi/6)\Delta\rho g d^3$. In the following, we therefore define the two dimensionless numbers as

$$\text{St} = \frac{1}{18\sqrt{2}}\frac{(\rho_p\Delta\rho g d^3)^{1/2}}{\mu_f}, \quad r = \left(\frac{\rho_p}{\rho_f}\right)^{1/2}, \tag{5}$$

assuming a constant drag coefficient C_D as in Ref. [3]. Thus, the Stokes number St prescribes the relative importance of particle inertia and fluid viscous effects while r is related to the fluid-grain density ratio. These two dimensionless numbers govern the grain dynamics in an elementary falling process and allow one to indicate the dominant process at the grain scale. According to the values of St and r, the three above-mentioned regimes can be obtained as follows. For St $\gg 1$ and $r \gg 1$, the ambient fluid has no effect on the dynamics of the granular avalanche and this is the free-fall regime, which corresponds usually to the well-known dry case. For St $\gg 1$ and $r \ll 1$, the gravity term is balanced by the inertial fluid drag force. The grain reaches its inertial limit velocity and is therefore associated with the inertial regime. It can be noted that the notation inertial regime refers here to a dominant contribution of fluid inertia to the dynamics, which is different from grain inertia. Moreover, in the case of immersed granular flows, the solid phase is usually denser than the fluid phase, r being therefore always larger than one and its smallest value of order one. A fully inertial regime is therefore not expected for a granular flow in this asymptotic consideration. However, a transition between a dry-dominated regime towards an inertial-dominated regime can be obtained for r decreasing to one [3]. For St $\ll 1$, the viscous effects are important and the grain reaches its Stokes limit velocity. This regime is thus referred to as the viscous regime.

In geophysical applications, the above-mentioned granular flow regimes can be encountered depending on grain and fluid characteristics [2]. Most dry granular flows in air, as rockfalls, subaerial landslides, or pyroclastic flows, lead to large values of the Stokes number and the grain-fluid density ratio, i.e., St $\sim [10^2, 10^8]$ and $r \sim 40$–50. These situations can be related to the free-fall regime, where the surrounding fluid can be neglected. In the case of submarine avalanches, the density ratio is

characterized by $r \sim 1.5$ while the Stokes number can be found in the large range of St $\sim [10^{-1}, 10^6]$. In these situations, the dynamics of the flow can belong to the inertial regime or the viscous regime, depending strongly on the grain size, and the influence of the fluid should therefore not be disregarded. Other atmospheric situations, such as snow avalanches or dust storms, can also lead to the situation of the inertial regime for which r remains moderate and St $\gg 1$. In several geophysical applications, such as lahars, some debris flows, and also snow avalanches under certain conditions, the interstitial fluid in the granular matrix differs from the ambient fluid. In these more complex situations, the influence of the surrounding fluids also has to be considered but leads to more complex physics including the density ratio and viscosity ratio between the two fluid phases. This reacher situation also suffers a lack of knowledge of the characteristics of the different regimes mentioned previously. The simpler case of the granular medium immersed in a single fluid still deserves specific attention.

In the literature, most studies of granular collapses deal with the free-fall regime [9–15,17,18,24–26]. The viscous regime has been investigated in detail by Rondon *et al.* [7], mostly focusing on the role of the initial volume fraction, while the inertial regime has only been mentioned in 2D numerical studies [8,27]. Laboratory experiments are therefore still needed to characterize the flow properties in these different regimes and their associated transition. For instance, the description of the regimes has been discussed in terms of the local dynamics of a single grain. Its influence on the macroscopic flow, involving a granular material as the collapse, is then still uncertain. In the light of the previous studies, the present work then focuses on an experimental description of the collapsing flow and the associated final deposit by varying the three independent dimensionless parameters (a, St, r). For the sake of clarity, the initial configuration considered here is always an initially dense-packing. Accordingly, the pore pressure induced by the initial decompaction of the granular medium prior flowing is negative [7].

The paper is organized as follows. In Sec. II the experimental setup and materials used are presented as well as observations of the granular collapse in a fluid. Then the scalings of the runout length and final height (Sec. III) and the spreading dynamics (Sec. IV) are described. Finally, a fine characterization of the morphology of the final deposit is given with the development of a simple predictive model (Sec. V).

II. LABORATORY EXPERIMENTS OF GRANULAR COLUMN COLLAPSE IN A FLUID

A. Experimental setup

The experiments are conducted in a horizontal transparent channel of rectangular cross section. The channel is 2 m long, 0.35 m high, and 0.20 m wide along with the streamwise x, vertical y, and spanwise z coordinates, respectively (see Fig. 1). On one side of the channel $x = 0$, a finite-volume reservoir is delimited by a sluice gate located at $x = L_i$. Two different reservoir widths are used, $L_i = 3$ and 10 cm. The initial height H_i of the granular column varies from 2 to 30 cm, leading to an aspect ratio $a = H_i/L_i$ in the range $a = [0.2, 10]$. At time $t = 0$, the sluice gate is removed and the granular column is released on the smooth bottom plane. The height profile $h(x, t)$ is extracted from image analysis using a classical shadowgraphy method. For this purpose, the 2D flow in the (x, y) plane is recorded using a Lavision 2560×2160 pixels camera and a backlight source on the opposite side of the channel. The obtained resolution is around $400 \ \mu\text{m pixel}^{-1}$, which leads to an accuracy of the height profile less than the grain diameter. The acquisition rate of the camera is between 10 and 200 Hz, depending on the flow timescale. The extraction process is performed using a MATLAB routine.

The granular medium is composed of spherical glass beads manufactured by Sigmund Lindner GmbH and listed as type S (soda lime glass beads) and type P (borosilicate glass beads). The measured densities of the beads are $\rho_p = 2500 \pm 50$ and $2230 \pm 30 \ \text{kg m}^{-3}$ and the grain diameters are $d = 3.15 \pm 0.3$ and 3.00 ± 0.02 mm, respectively. In the dry case, type S grains of diameter $d = 1.15 \pm 0.15$ mm have also been used. For all types of particles, the repose and avalanche angles were estimated using two methods. First, the variation of the slope, along a granular pile built by

TABLE I. Set of parameters for each experimental series. The Stokes number St and the fluid-grain density ratio r are defined according to (5).

Glass beads	Ambient fluid	St	r	Regime	Label
$d = 1$ mm $\rho_p = 2500$ kg m^{-3}	$\mu_f = 1.8 \times 10^{-5}$ Pa s $\rho_f = 1.2$ kg m^{-3}	540	46	free-fall	FF
$d = 3$ mm $\rho_p = 2230$ kg m^{-3}	$\mu_f = 1.8 \times 10^{-5}$ Pa s $\rho_f = 1.2$ kg m^{-3}	2500	43	free-fall	FF
$d = 3$ mm $\rho_p = 2230$ kg m^{-3}	$\mu_f = 10^{-3}$ Pa s $\rho_f = 1000$ kg m^{-3}	33	1.5	inertial	I
$d = 3$ mm $\rho_p = 2500$ kg m^{-3}	$\mu_f = 26 \times 10^{-3}$ Pa s $\rho_f = 1027$ kg m^{-3}	1.5	1.6	viscous inertial	VI
$d = 3$ mm $\rho_p = 2500$ kg m^{-3}	$\mu_f = 375 \times 10^{-3}$ Pa s $\rho_f = 1066$ kg m^{-3}	0.1	1.5	viscous	V

slowly pouring beads just above the top of the pile, was considered as being delimited by these two angles. The second method consists in slowly tilting a rectangular plexiglass box, initially filled with a horizontal granular bed of height of a few grains. Using these two methods, the angle of repose and the angle of avalanche were found to be $\alpha_r = 22 \pm 1°$ and $\alpha_a = 28 \pm 2°$, respectively. In this study, the initial volume fraction of the granular column is constant and equal to $\phi \sim 64 \pm 2\%$, i.e., a dense-packing, for all experiments considered here. The influence of the initial volume fraction in the viscous regime has already been reported by Rondon *et al.* [7] and it is therefore not discussed further here.

For collapse experiments with a liquid phase, the channel is filled up to a height equal to about 35 cm with a mixture of water and Ucon oil 75H90000. The dynamic viscosity of this mixture depends on the relative concentration of Ucon oil and water, which is characterized by the mass fraction $c_m = m_o/(m_o + m_w)$, with m_o and m_w the mass of oil and water, respectively. The mass fraction c_m is varied from 0% (pure water) to 40%, which corresponds to a variation of viscosity in the range $\mu_f = [1,375]$ cP. The viscosity of the fluid mixture is obtained by rheometric measurements using a cone-plate geometry in a Haake Mars III rheometer with an accuracy less than 5%. Also, the fluid density is measured by a DMA 35 Anton Paar electronic densimeter with an accuracy of ± 0.5 kg m^{-3}.

Table I lists the set of fluid and grain properties used in the experiments. According to the definitions (5), St and r are constant for a given set of fluid-grain properties (reported in Table I) and they are therefore varied independently of the value of a. Series of experiments are labeled according to the expected flow regime depending on the (St,r) values and defined by Courrech du Pont *et al.* [3]. In particular, the different series of experiments performed in the present study will be referred to as regime FF in the free-fall regime, regime I in the inertial regime, regime V in the viscous regime, and regime VI at the transition between the viscous and the inertial regimes (see Table I for details of the fluid mixture and grain properties). The corresponding values of (St,r) are reported in Table I and the series of experiments are also represented by a symbol in the (St,r) plane in Fig. 2.

B. Observations of the granular collapse

The typical evolution of the granular collapse for regime FF, regime V, and regime I is shown for three different aspect ratios $a = 0.5$, 1, and 9, in Fig. 3. In particular, snapshots of the granular flow at $t_f/3$, $2t_f/3$, and t_f, with t_f the final time at which the granular medium comes to rest, are reported. See also the available movies corresponding to granular collapses for regime FF, regime V, and regime I, with a constant aspect ratio, i.e., $a = 1$. In the latter case, a granular collapse at large aspect ratio, i.e., $a = 9$, is also shown [28].
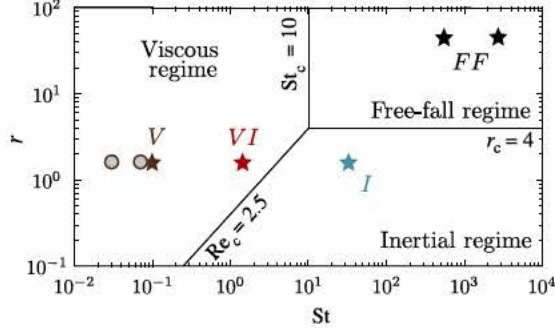
FIG. 2. Granular-fluid flow regimes in the (St,r) plane according to (5). Stars and circles correspond to the experimental series performed in the present study and in Ref. [7], respectively.

One can first note that the shape of the final deposit depends on both the aspect ratio a and the considered regime (St,r). More specifically, a affects the trapezoidal vs triangular shape according to the definition of [7] for the range of parameters considered here. Note that even if the final deposit can be clearly simplified to such simple geometries in regime V, the final deposit shape is slightly more curved at the front for the two other regimes, i.e., regimes FF and I. Curvature of the final shape deposit can therefore be attributed to inertia in the dynamics of the granular-fluid flow. However, a clear distinction can be made between two situations such as $h(x = 0, t = t_f) = h(0, 0)$ (referred to as a trapezoid) and $h(0, t_f) < h(0,0)$ (referred to as a triangle). Using this formalism, the transition from the trapezoid to the triangle occurs around $a \sim 0.75$, in the range of parameters considered here. Note that St and r have probably a small influence on this transition, but it is difficult to conclusively determine this specific dependence. However, at each a, the spreading length clearly increases with
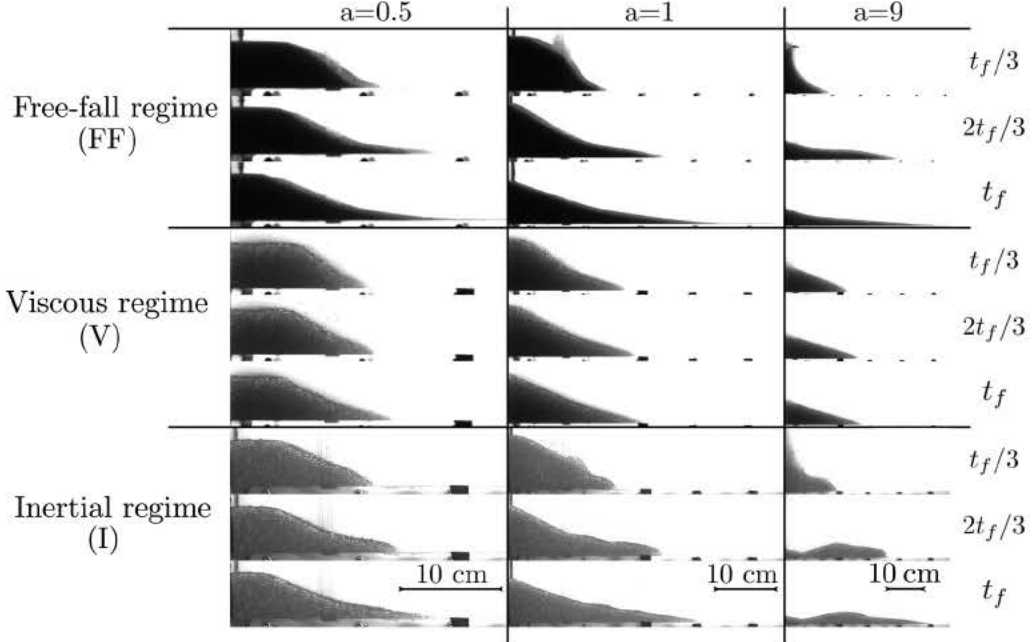

FIG. 3. Snapshots of the granular collapse for regime FF, regime V, and regime I for three different aspect ratios and at three different times.
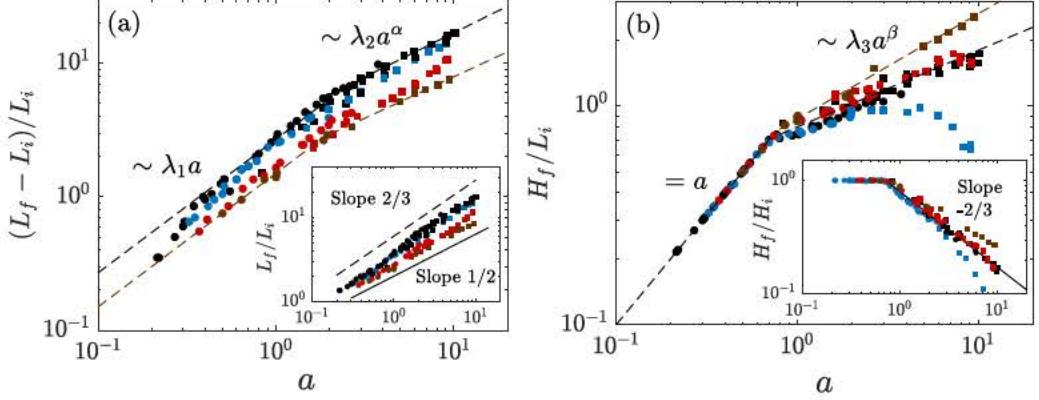
FIG. 4. (a) Dimensionless runout length $(L_f - L_i)/L_i$ (inset L_f/L_i) and (b) final height H_f/L_i (inset H_f/H_i) as a function of the aspect ratio a for regime FF (black), regime I (blue), regime VI (red), and regime V (brown). Circles and squares correspond to experiments performed with reservoir widths of $L_i = 10$ and 3 cm, respectively.

St while the effect of r is marginal on this length. In fact, the influence of r is more clearly observed in the transient flow which highlights a thicker front for $r \sim 1.5$ (second and third rows) than for $r \sim 45$ (first row), whatever a. This effect of r on the front thickness is comparable to the case of a pure fluid gravity current (i.e., the intrusion of a heavy fluid in a lighter fluid) which exhibits a similar front shape difference between a large density ratio, well known as dam break flows, and a smaller density ratio [29,30]. To conclude, one can notice that regime I highlights specific surface shapes during the transient flow (see $a = 1$ in Fig. 3) and even on the final deposit (see $a = 9$ in Fig. 3). In the latter case, a deposit somehow similar to the Mexican-hat structure observed for fluidized [20,31] and nonfluidized [14,15,17,26] dry collapses is obtained. Note, however, that in nonfluidized dry cases, this specific deposit is usually observed at larger a.

These observations highlight the diversity of behaviors which can be obtained for the collapse of granular column in a liquid, clearly controlled by the dimensionless parameters (a, St, r). The influence of these dimensionless parameters on both the dynamics of the front and the final deposit shape are more deeply investigated in the following.

III. RUNOUT LENGTH AND FINAL HEIGHT

Following previous studies on dry granular collapses, the final deposit is characterized by its runout length L_f, which is the final front position at $y = 0$, and its final height H_f corresponding to the height of the granular material at $x = 0$. Figure 4 shows these two quantities, in a dimensionless form, as a function of the initial aspect ratio a for regime FF (black symbols), regime I (blue symbols), regime VI (red symbols), and regime V (brown symbols), respectively. In particular, the classical dimensionless runout length $(L_f - L_i)/L_i$ [Fig. 4(a)] and final height H_f/L_i [Fig. 4(b)] as well as L_f/L_i [inset of Fig. 4(a)] and H_f/H_i [inset of Fig. 4(b)] are shown. As often observed for the dry granular collapse, these dimensionless lengths highlight a power-law dependence on a with distinct behaviors at small and large a (see Sec. I). This trend is recovered here for the different regimes even if some unexpected features are observed, particularly for regimes I and VI, which will be discussed more thoroughly further on in the paper. The runout length is shown here to be restricted to a range of values bounded by the dry regime (regime FF) on the upper side and the viscous regime (regime V) on the lower side [see Fig. 4(a)]. These two limiting curves highlight scaling laws depending on a. In particular, for $a \lesssim 2$, the runout length increases linearly with the aspect ratio, $(L_f - L_i)/L_i = \lambda_1 a$ with $\lambda_1 = \lambda_1^{\mathrm{FF}} \sim 2.7 \pm 0.3$ and $\lambda_1 = \lambda_1^{\mathrm{V}} \sim 1.5 \pm 0.1$ for regimes FF and V, respectively. For $a \gtrsim 2$, the runout length evolves as $(L_f - L_i)/L_i = \lambda_2 a^{\alpha}$ with $\alpha \sim 0.64 \pm 0.02$ and $\lambda_2 = \lambda_2^{\mathrm{FF}} \sim 3.7 \pm 0.3$
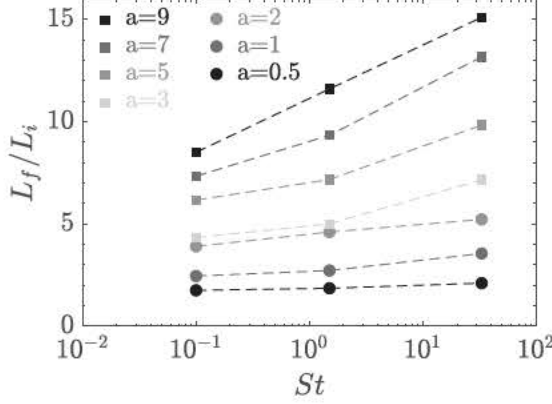
FIG. 5. Dimensionless runout L_f/L_i as a function of St for $r \sim 1.5$ and $a = [0.5,9]$. Circles and squares correspond to experiments performed with reservoir widths of $L_i = 10$ and 3 cm, respectively.

and $\lambda_2 = \lambda_2^V \sim 1.9 \pm 0.1$ for regimes FF and V, respectively. An important observation that can be made is that the runout length is significantly shorter in regimes V and VI than in regimes FF and I, highlighting the St dependence mentioned in the preceding section, while the exponent α does not vary significantly. Another scaling which has been shown to be pertinent to characterize the final length of the collapse, at least for a triangle deposit, is the dimensionless length L_f/L_i [7]. The scaled runout length L_f/L_i is plotted as a function of a for the different regimes in the inset of Fig. 4(a). Again, the overall trend is similar for the different regimes. In regime V, one obtains $L_f/L_i \sim a^{1/2}$, in accord with previous results in the literature [7]. More surprisingly, this scaling also looks pertinent for the other regimes, at least for the dry case, but with a varying scaling factor between small a and large a. Unfortunately, these scaling laws for the runout remains a challenging task, as the range of a that can be covered in laboratory experiments is limited [see the 2/3 power law reported in the inset of Fig. 4(a), which is hardly distinguished from a 1/2 power law].

Figure 4(b) shows the dimensionless final height H_f/L_i as a function of the aspect ratio a. For $a \lesssim 0.75$, the final deposit has a trapezoidal shape leading to $H_f = H_i$. The initial height at $x = 0$ is therefore not affected by the collapse. For $a \gtrsim 0.75$, the trend is more complicated and it can depend on the considered regime. However, except for regime I, H_f/L_i evolves as $H_f/L_i = \lambda_3 a^\beta$, with $(\lambda_3, \beta) = (\lambda_3^{FF}, \beta^{FF}) = (\lambda_3^{VI}, \beta^{VI}) = (0.80 \pm 0.07, 0.35 \pm 0.04)$ and $(\lambda_3, \beta) = (\lambda_3^V, \beta^V) = (0.87 \pm 0.03, 0.48 \pm 0.02)$. In regime I, H_f/L_i is similar to the case of regimes FF and VI for $a \lesssim 2$. For $2 \lesssim a \lesssim 5$, it remains constant and then decreases with a at larger aspect ratio. The former observation clearly highlights the influence of r at large St on the final deposit mentioned in Sec. II B. The inset of Fig. 4(b) shows the dimensionless final height H_f/H_i as a function of a. For $a \lesssim 0.75$, the trapezoidal shape leads to $H_f/H_i = 1$, while for $a \gtrsim 0.75$, H_f/H_i decreases with a following different slopes depending on the considered regime. The $-2/3$ scaling obtained for dry granular collapses in the quasi-2D geometry [13] is reported here for comparison [solid black line in the inset of Fig. 4(b)]. A comparison with results obtained by Rondon et al. [7], in the case of a viscous regime for different initial volume fraction ϕ, is detailed in the Appendix. Surprisingly, it shows that decreasing ϕ (constant St) or increasing St (constant ϕ) leads to similar behaviors regarding the scaling laws of the final runout. It therefore opens the way to several discussions of the role of the pore pressure on the global dynamics of the collapse. With the set of experiments obtained by Rondon et al. [7], Roche et al. [20], and the present study, it would require specific attention to conclusively determine this role.

In Fig. 5, the dependence of the dimensionless runout length L_f/L_i on the Stokes number St is shown. Here the grain-fluid density ratio is fixed, i.e., $r \sim 1.5$, and the aspect ratio is in the range $a = [0.5,9]$. As already mentioned, the spreading length quantified as L_f/L_i increases with St and
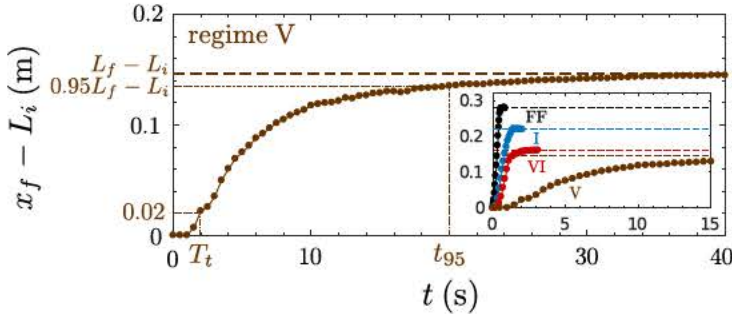
FIG. 6. Temporal evolution of the front position $x_f - L_i$ for regime V; the inset shows a comparison for regime FF (black), regime I (blue), regime VI (red), and regime V (brown), with $a = 1$. The dashed lines represent the runout length $L_f - L_i$. The trigger time T_t and the time t_{95} are indicated.

the evolution is more pronounced at large a. Moreover, while L_f/L_i roughly increases by a factor 5 when a is increased over a decade, it only increases by a factor 2 or less when St is varied over three decades, explaining probably why the influence of the aspect ratio has been more widely reported in the literature than the influence of the Stokes number. However, in geophysical applications, St can vary over several decades depending on the density and size of the grains (see Sec. I), its influence on the spreading length therefore being significant.

IV. DYNAMICS OF THE SPREADING

A. Flow regimes and physical processes

The dynamics of the granular flow is analyzed here through the temporal evolution of the front position. In particular, the position $x_f - L_i$ is plotted as a function of the time for regime V with $a = 1$, in Fig. 6, as a typical example of this evolution. A comparison with the other regimes is also shown in the inset of Fig. 6 with regime FF (black symbols), regime I (blue symbols), regime VI (red symbols), and regime V (brown symbols).

This evolution is decomposed into the following stages. First, the front remains nearly frozen from $t = 0$, i.e., the opening of the sluice gate, to $t = T_t$, referred to as the trigger time. Here the trigger time T_t is defined as the time at which the front has traveled on the width of the sluice gate [i.e., $x_f(t = T_t) - L_i = 2$ cm]. This extraction method allows an objective measurement without affecting significantly the results discussed in the following. Then the most significant evolution of the granular medium occurs during a second stage, i.e., the collapse phase, until the front reaches its maximum length L_f, i.e., the granular media stops. In order to quantify the end of the second stage of the collapse, we define the time t_{95} when the front position of the collapse reaches 95% of the runout length L_f (see Fig. 6). The two above-mentioned times T_t and t_{95} clearly decrease with increasing (St,r), i.e., from regime V to regime FF, leading to a smooth or a sharp trend of the front evolution (see the inset of Fig. 6).

For the first stage, the trigger time T_t is similar to the one mentioned by Rondon et al. [7] in the case of an initial dense granular packing. We recall here that the initial packing of each experiment is constant with $\phi \sim 64\%$. This time is related to the time that the granular column needs to expand prior to collapse. This expansion is delayed by the viscous dissipation in the granular porous media. Figure 7(a) shows the trigger time T_t as a function of the initial height H_i for regime FF (black symbols), regime I (blue symbols), regime VI (red symbols), and regime V (brown symbols). One can conclude that T_t is nearly H_i independent, i.e., independent of a in the range of parameters considered here, and that it is mostly controlled by the flow regime, i.e., (St,r). A constant value $\langle T_t \rangle$ [dashed lines in Fig. 7(a)] can be therefore defined in each regime which is reported as a function of St in Fig. 7(b). Note that in the present set of experiments it was not possible to vary the grain-fluid
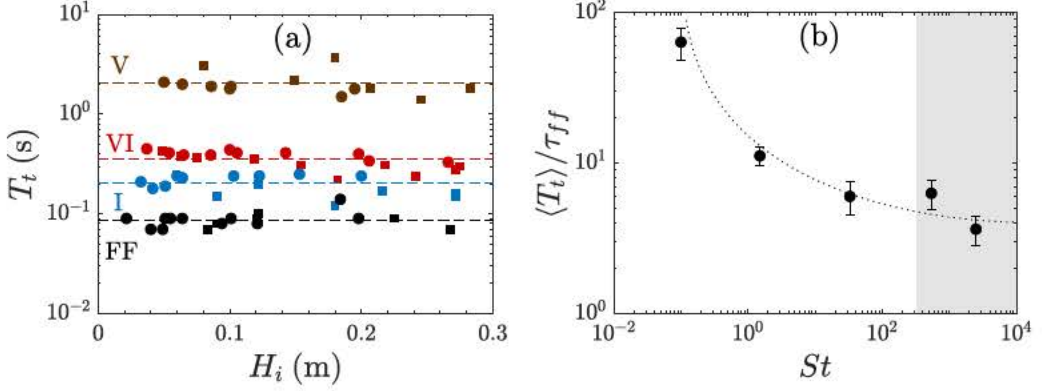
FIG. 7. (a) Trigger time T_t as a function of the initial height H_i for regime FF (black), regime I (blue), regime VI (red), and regime V (brown). The dashed lines represent the mean value $\langle T_t \rangle$ for each regime. (b) Dimensionless trigger time $\langle T_t \rangle / \tau_{ff}$, with $\tau_{ff} = (2\rho_p d / \Delta \rho g)^{1/2}$, as a function of the Stokes number St. The white and gray areas correspond to experiments with $r \sim 1.5$ and 45, respectively.

density ratio r at a constant value of the Stokes number St; thus no conclusions could be drawn about the influence of r, even if it does not seem to significantly modify the trigger time at large St in the range of parameters considered here [see Fig. 7(b) in which white and gray areas correspond to $r \sim 1.5$ and 45, respectively]. However, a clear dependence on St is obtained here. In particular, the trigger time $\langle T_t \rangle / \tau_{ff}$, where $\tau_{ff} = (2\rho_p d / \Delta \rho g)^{1/2}$ is the free-fall timescale of a grain over d, is shown to decrease with increasing St. This observation is then consistent with a viscous dissipation during the expansion which is significant at small St and tends towards unity, i.e., the free-fall timescale, at large St. The influence of a dense packing on the initial stage of the collapse reported by Rondon *et al.* [7] for a viscous regime (i.e., at low St) can then be quantified as a function of St. Note that the asymptotic value obtained at large St, $\langle T_t \rangle / \tau_{ff} \sim 3$, slightly above one, is affected by the measurement method of the trigger time described previously. Nevertheless, the general trend reported here remains robust.

The second stage of the collapse is characterized by the time t_{95} prior to the granular medium coming to rest. Strictly speaking, the second stage lasts for $t_{95} - T_t$ and we consider this time difference in the following. In order to validate the relevance of the different regimes mentioned previously for this configuration, we thus analyzed the evolution of $t_{95} - T_t$ as a characteristic timescale of the granular collapse. As discussed by Courrech du Pont *et al.* [3], the time of the granular collapse should depend on the corresponding regime. It should therefore be predicted according to the considered flow regime. If we consider $U_{V(I)}^\infty$ the limit velocity that a single grain reaches when it is submitted to a driving force F in the viscous (inertial) regime and the characteristic length L_c traveled during the collapse time, the characteristic time can be defined as $T_V = L_c / U_V^\infty = 3\pi \mu_f d L_c / F$ and $T_I = L_c / U_I^\infty = L_c (\pi C_D \rho_f d^2 / 8F)^{1/2}$ for the viscous regime and inertial regime, respectively. In the case of the free-fall regime, as no limit velocity exists, the characteristic time is defined as $T_{FF} = (L_c \rho_p \pi d^3 / 3F)^{1/2}$, which corresponds to the time that a particle needs to travel on the characteristic length L_c with a constant acceleration induced by a constant force F. In order to predict simple scalings for these characteristic times from the initial condition, we choose here $L_c = H_i$, i.e., the initial height, and $F = (\pi/6)\Delta \rho g d^3$, i.e., the weight of a single grain. Note that with these definitions, one has simply $T_{FF} = (H_i / d)^{1/2} \tau_{ff}$. We therefore obtain

$$T_{FF} = \left(\frac{2\rho_p H_i}{\Delta \rho g} \right)^{1/2}, \quad T_I = \left(\frac{3 C_D \rho_f H_i^2}{4 \Delta \rho g d} \right)^{1/2}, \quad T_V = \frac{18 \mu_f H_i}{\Delta \rho g d^2}. \quad (6)$$

The time $t_{95} - T_t$ normalized by these different characteristic times (6) is plotted as a function of the normalized initial height H_i / d for regime FF (black symbols), regime I (blue symbols), regime VI
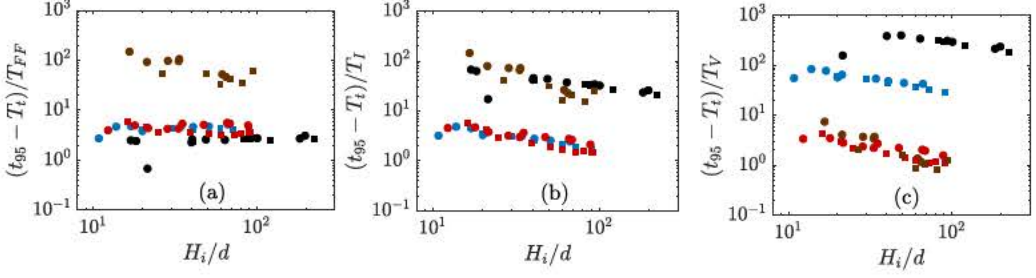
FIG. 8. Dimensionless collapse time $t_{95} - T_t$ as a function of the normalized initial height H_i/d for regime FF (black), regime I (blue), regime VI (red), and regime V (brown). The characteristic times T_{FF}, T_I, and T_V are defined according to (6). Circles and squares correspond to experiments performed with reservoir widths of $L_i = 10$ and 3 cm, respectively.

(red symbols), and regime V (brown symbols) in Fig. 8. The drag coefficient is considered constant, i.e., $C_D = 0.4$, according to the definition given by Cassar *et al.* [4], corresponding to the value of C_D of a single sphere in a uniform flow at large particle Reynolds number [32]. One can conclude from Fig. 8 that the collapse time for regimes FF and V only scales with T_{FF} and T_V, respectively (black and brown symbols in Fig. 8), supporting the expected classification proposed by Courrech du Pont *et al.* [3] in these cases. On the other hand, it is more difficult to conclude for regimes I and VI, for which the timescale is not clear. For regime I, the time T_I seems to be as pertinent as the time T_{FF}, at least at small a, meaning that T_I and T_{FF} are of the same order, with in particular $T_{FF} \sim T_I \sim 0.1$ s, obtained here from (6) with the present set of parameters. For regime VI, it is not surprising to obtain that both T_V and T_I are of the same order, with $T_V \sim T_I \sim 0.1 - 1$ s in this case, as these two timescales should be similar at the transition from viscous to inertial regimes. Also, T_{FF} is of the same order as T_I and T_V in this case ($T_{FF} \sim 0.1$ s), in agreement with previous conclusions mentioned for regime I. It is worth mentioning that the smallest value of the fluid-grain density ratio considered here is $r \sim 1.5$ (glass beads in a liquid). More specifically, for regimes VI and I, that means the inertial limit velocity is hardly reached between consecutive grain contacts, according to the definition (5) of the density ratio. In fact, regime I is at the limit between the inertial and free-fall regimes, while regime VI is close to the point of coexistence of the three regimes. For heavy grains and at large St, the flow is then never expected to belong to a regime in which fluid inertia overcomes significantly the weight of the grains. Usually, the granular medium remains quite dense during the whole duration of the collapse, which explains the similarity between regimes I and FF.

Nevertheless, beyond this general observation, Fig. 3 showed that the dynamics and the final deposit of the granular collapse could highlight the observable difference between regimes FF and I. For instance, at large a, more particles are evacuated from the initial reservoir in regime I compared to regime FF, leading to a bulge of the final deposit surface. In this way, this suggests that fluid inertia should be observable and quantified, at least for large a. In fact, the conclusions drawn previously do not account for the H_i dependence observed in Figs. 8(b) and 8(c). For instance, in regime I and at large H_i/d, the collapse time $t_{95} - T_t$ decreases towards the expected time T_I [see blue symbols in Fig. 8(b), in which $(t_{95} - T_t)/T_I$ tends to 1 when H_i/d increases] while it remains always larger that T_{FF} independently of H_i/d [see blue symbols in Fig. 8(a)]. In this case, fluid inertia becomes dominant when increasing H_i/d and this can be explained as follows. At large H_i/d, most of the column falls down only in the vertical direction due to the mass of grains drained away at the bottom during the collapse, as reported by Staron and Hinch [14]. During this stage, the intensity of the contact network can be expected to vanish as particles fall similarly. In this case, the definitions of the Stokes number St and the fluid-grain density ratio r [Eq. (5)] given in Sec. I are no longer pertinent. Indeed, the viscous time and the inertial time that a grain needs to reach its limit velocity now have to be compared to a free-fall time over the total height of the initial column H_i, instead of the grain diameter d. In this case, the zone of influence of the different regime has to be discussed in
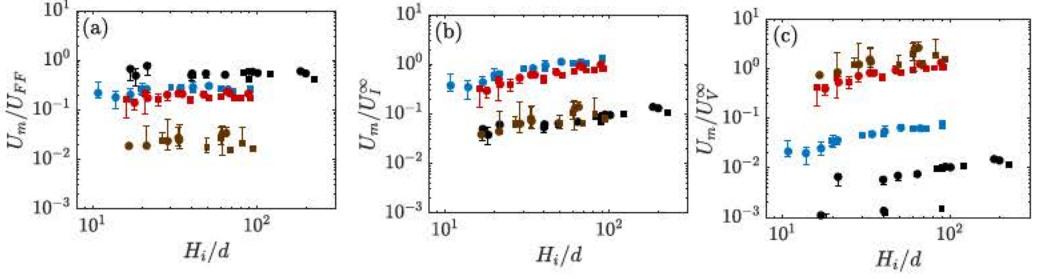
a

FIG. 9. Maximum front velocity U_m normalized by different characteristic velocities U_{FF}, U_I^∞, and U_V^∞ defined according to (7) as a function of the normalized initial height H_i/d for regime FF (black), regime I (blue), regime VI (red), and regime V (brown).

$((d/H_i)^{1/2}\text{St},(d/H_i)^{1/2}r)$ plane. Then, for a series of experiments with a constant (St,r), $(d/H_i)^{1/2}r$ decreases with the increase of the initial height H_i and the flow could then reach its inertial regime as long as $(d/H_i)^{1/2}\text{St}$ remains large. For regime VI, the same conclusions can be drawn. In this case, $(d/H_i)^{1/2}\text{St}$ and $(d/H_i)^{1/2}r$ decrease similarly, explaining that it remains at the limit between the viscous and inertial regimes while it separates from the free-fall dynamics at large H_i/d.

Note that to confirm the previous description of the dynamics based on the collapse timescale, the maximum front velocity U_m reached during the granular flow can also be analyzed in a similar way. In each regime considered, the evolution of the front velocity can be defined as an acceleration followed by a deceleration and no constant-velocity phase is observed (not shown here), as reported by Staron and Hinch [17] in the dry case. In the following, we define the velocity scales as the limit velocity $U_{V(I)}^\infty$ in the viscous (inertial) regime and the characteristic velocity U_{FF}, at $t = T_{FF}$, considering the fall of a single grain under gravity and without drag dissipation. We therefore obtain

$$U_{FF} = \left(\frac{2\Delta\rho g H_i}{\rho_p}\right)^{1/2}, \quad U_I^\infty = \left(\frac{4\Delta\rho g d}{3C_D\rho_f}\right)^{1/2}, \quad U_V^\infty = \frac{\Delta\rho g d^2}{18\mu_f}. \tag{7}$$

Figure 9 shows the maximum front velocity U_m normalized by the velocity scales defined according to (7) as a function of the normalized initial height H_i/d for regime FF (black symbols), regime I (blue symbols), regime VI (red symbols), and regime V (brown symbols). The trends are similar to the one observed for the characteristic times. The same conclusions can be drawn which support the physical interpretation given previously on the flow dynamics of the collapse.

These results are now summarized in the $((d/H_i)^{1/2}\text{St},(d/H_i)^{1/2}r)$ plane to support the previous discussion. First, in order to identify the most pertinent granular flow regime for each experiment performed in this study, we define the minimum dimensionless timescale as

$$T^- = \min\left[\frac{t_{95} - T_t}{T_{FF}}, \frac{t_{95} - T_t}{T_I}, \frac{t_{95} - T_t}{T_V}\right]. \tag{8}$$

The value of T^- can be extracted from Fig. 8. As all the ratios in the definition (8) are larger than one, the value of T^- then corresponds to the ratio whose value is closest to one. This therefore gives us first the most pertinent regime according to the minimum ratio obtained and then a quantification of its relevance according to the value of T^-, with an increasing confidence of the relevance when T^- is actually reaching one. It can be noted that a similar approach could be done with the maximal front velocity U_m leading to the same conclusions. Figure 10 shows the regimes obtained in the $((d/H_i)^{1/2}\text{St},(d/H_i)^{1/2}r)$ plane. Symbols correspond to each individual experiment in this parameter space. In particular, black symbols, blue symbols, and brown symbols correspond to $T^- = (t_{95} - T_t)/T_{FF}$, $T^- = (t_{95} - T_t)/T_I$, and $T^- = (t_{95} - T_t)/T_V$, respectively. The size indicates the deviation of T^- from 1, in particular, the size of the symbol increases when $T^- \to 1$. Note that, in such a representation, each set of experiments for regimes FF, I, VI, and V are still visible (symbols align on

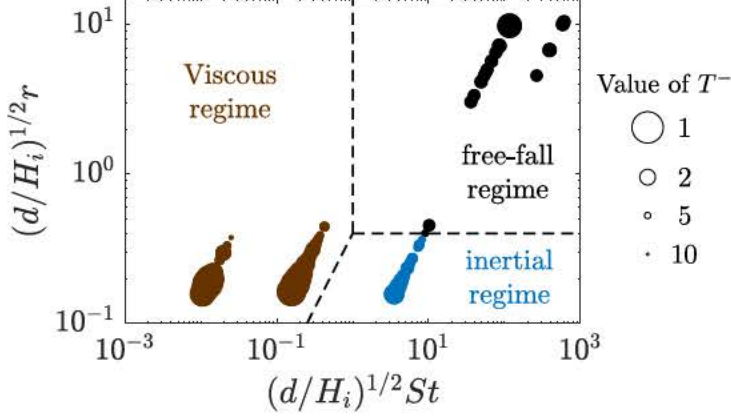FIG. 10. Granular flow regimes in the $((d/H_i)^{1/2}\mathrm{St},(d/H_i)^{1/2}r)$ plane with St the Stokes number and r the grain-fluid density ratio defined according to (5). Symbols (colors and sizes) correspond to the minimum dimensionless collapse time T^- according to (8) and determined from Fig. 8 with, in particular, black symbols for $T^- = (t_{95} - T_t)/T_{\mathrm{FF}}$, blue symbols for $T^- = (t_{95} - T_t)/T_{\mathrm{I}}$, and brown symbols for $T^- = (t_{95} - T_t)/T_{\mathrm{V}}$. The size indicates the deviation of T^- from 1 (see the legend).

inclined lines). Then, in this parameter space, a change in color indicates a transition from one regime to another, while the size of the symbols indicates the distance to this transition. It can be noted that the set of experiments for regimes FF and V indeed belongs to the corresponding expected regime. Regime VI belongs to a viscous regime with this definition. Moreover, the size of the symbols are observed to decrease when approaching transitions from one regime to another. One of the most interesting observations with this representation is associated with the set of experiments initially denoted as regime I according to the definition of (St, r) at the grain scale [Eqs. (5)], which is now shown to cross the transition from the inertial to the dry regime as $((d/H_i)^{1/2}St, d/H_i^{1/2}r)$ increases (see blue and black symbols in the bottom right pannel of Fig. 10). Figure 10 then allows us to extract a more refined estimation of the transition in this new $((d/H_i)^{1/2}\mathrm{St},(d/H_i)^{1/2}r)$ plane for the collapse configuration, with in particular $(d/H_i)^{1/2}r_c \sim 0.4$ from free-fall to inertial regimes, $(d/H_i)^{1/2}\mathrm{St}_c \sim 1$ from free-fall to viscous regimes, and $\mathrm{Re}_c = \mathrm{St}_c/r_c \sim 2.5$ from inertial to viscous regimes, in agreement with the critical Reynolds number suggested by Courrech du Pont et al. [3].

B. Simple St scaling of the flow dynamics: A geophysical purpose

The description of geophysical flows necessitates the use of simple parametrizations modeling the main features of the physical processes involved in the configuration considered. In this sense, the results shown in Figs. 8(a) and 9(a) suggests a possible rough description of the dynamics of granular avalanches in a fluid with a classical free-fall scaling, at least for regimes FF, I, and VI and in the range of parameters considered here, regardless of the finer description proposed previously. Indeed, these scalings are already used relevantly in many gravity-driven flows such as gravity currents, dam break flows, dry granular collapses, or even fluidized granular flows [13,23,30,33]. In Fig. 11(a), U_m is thus plotted as a function of the free-fall velocity $U_{\mathrm{FF}} = (2\Delta\rho g H_i/\rho_p)^{1/2}$ for regime FF (black symbols), regime I (blue symbols), regime VI (red symbols), and regime V (brown symbols). It is indeed shown here that such a free-fall scaling for the velocity remains roughly acceptable for all the experiments performed here [see the dashed lines in Fig. 11(a), which all have a slope 1, i.e., corresponding to a linear dependence of U_m with U_{FF}]. The prefactor of this scaling (i.e., the prefactor associated with the linear trend of each dashed line) would therefore only be a function of St, i.e., $U_m = \zeta(St)U_{\mathrm{FF}}$. The evolution of ζ as a function of St is shown in Fig. 11(b). It can be observed that ζ decreases with decreasing St, which quantifies the viscous dissipation in the system. Extrapolating the trend observed in Fig. 11(b), ζ could be found to about 1, for St $\sim 10^6$, which is the upper value usually
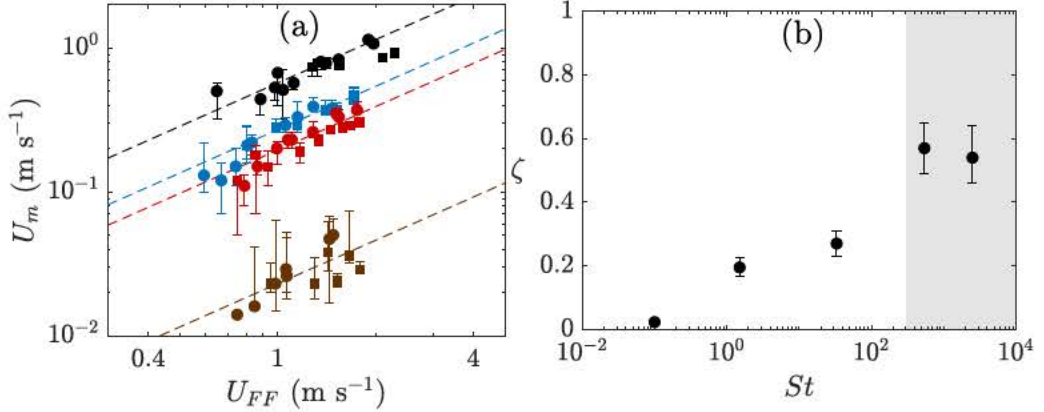
FIG. 11. (a) Maximum front velocity U_m as a function of the free-fall velocity $U_{FF} = (2\Delta\rho g H_i/\rho_p)^{1/2}$ for regime FF (black), regime I (blue), regime VI (red) and regime V (brown). (b) Evolution of $\zeta = U_m/U_{FF}$ as a function of the Stokes number St. The parameter ζ is obtained from the prefactor of the linear fit [dashed lines in Fig. 11(a)]. White and gray areas correspond to $r \sim 1.5$ and 45, respectively.

obtained for dam break flows for which the influence of viscous and/or frictional dissipation is small (as gravity current, turbidity current, or fluidized bed [23], for instance). Below St ~ 0.1, the velocity of the system is found to be zero. It is actually the limit of the assumptions used here; the system can then be considered as fully viscous. While ζ is clearly a function of St here, it could also depend on r [see Fig. 11(b), in which white and gray areas correspond to $r \sim 1.5$ and 45, respectively], but cannot be highlighted with the set of available parameters. Such a rough description accounts for the simplest influence of the surrounding fluid on the dynamics of a granular mass slumping under the influence of the gravity standing for a classical free-fall scaling for inertial or dry configurations towards the dissipation induced by viscosity. This parametrization would need further investigation, which is beyond the scope of the present paper, to propose a robust correlation for the function $\zeta(St,r)$ and the range of parameters of validity. This could probably only be achieved with numerical simulations.

V. MORPHOLOGY OF THE FINAL DEPOSIT

In the previous sections, the influence of the dimensionless numbers (a,St,r) has been shown to play a role in the dynamics of a granular collapse and/or the shape of the final deposit obtained. In this section, the morphology of the final deposit is characterized in the range of parameters considered. In Fig. 12, the characteristics of the final deposit are recalled for a trapezoidal form, with the final height H_f and the runout length L_f, the angles α_s and α_f at the summit and at the foot, respectively, and x_c corresponding to the longitudinal position of transition from a constant height profile to a decreasing height profile ($x_c = 0$ for a triangular deposit).
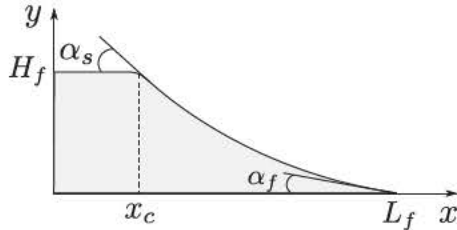

FIG. 12. Sketch of a final trapezoidal deposit with the runout length L_f and the final height H_f, the angles α_s and α_f at the summit and at the foot, respectively, and x_c corresponding to the longitudinal position of transition from a constant height profile to a decreasing height profile.
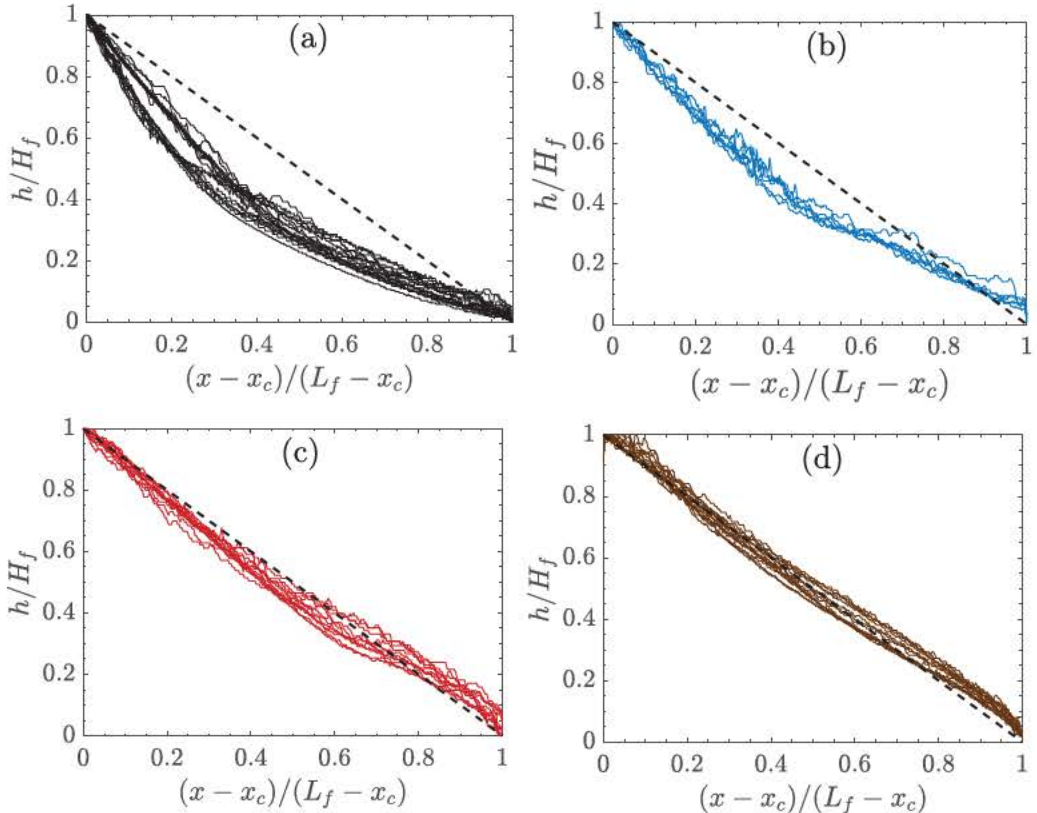
FIG. 13. Height profile h/H_f as a function of $(x - x_c)/(L_f - x_c)$ for (a) regime FF, (b) regime I, (c) regime VI, and (d) regime V. The dashed lines represent $h/H_f = 1 - (x - x_c)/(L_f - x_c)$.

A. Shape of the deposit

The shape of the final deposit can be regarded as a function of the regime considered. Figure 13 shows the height profile h/H_f as a function of $(x - x_c)/(L_f - x_c)$ for regime FF [Fig. 13(a)], regime I [Fig. 13(b)], regime VI [Fig. 13(c)], and regime V [Fig. 13(d)]. All the aspect ratios are reported here except in regimes I and VI for which a is limited to $a \lesssim 1$ and 4, respectively. For these two sets of experiments, spatial oscillation of the granular surface appears above these aspect ratios. This specific situation will be discussed in more detail in Sec. V C. In Fig. 13, one can first observe that, in each case, these dimensional height profiles nearly match on a single curve for all a. Moreover, for decreasing St, these self-similar profiles tend towards a straight line [from Figs. 13(a)–13(d)], i.e., a constant angle along the slope of the deposit (dashed lines).

The center of mass (x^G, y^G) can be analyzed as a quantification of this similarity in the final deposit and it is defined as

$$x^G = \frac{1}{A} \int_0^{x_f} x h(x,t) dx, \quad y^G = \frac{1}{A} \int_0^{x_f} \frac{h(x,t)^2}{2} dx, \qquad (9)$$

where x^G and y^G are the longitudinal and vertical positions of the center of mass and $A = \int_0^{x_f} h(x,t) dx$ is the area of the granular material. Initially at the position $(x^G(t=0), y^G(t=0)) = (L_i/2, H_i/2)$, the longitudinal position x^G increases while the vertical position y^G decreases during the spreading of the granular mass until it stops at the position of the final state (x^G_f, y^G_f).
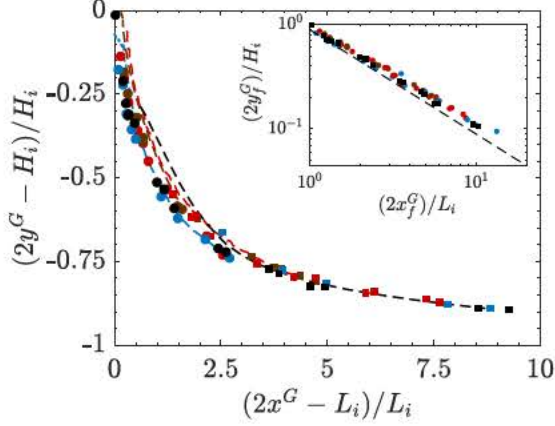
FIG. 14. Dimensionless vertical position of the mass center $(2y^G_f - H_i)/H_i$ as a function of its horizontal position $(2x^G_f - L_i)/L_i$ for regime FF (black), regime I (blue), regime VI (red), and regime V (brown). Symbols correspond to the final state $((2x^G_f - L_i)/L_i, (2y^G_f - H_i)/H_i)$ while the dashed lines correspond to the temporal trajectory $((2x^G - L_i)/L_i, (2y^G - H_i)/H_i)$ of the center of mass. The inset corresponds to $2y^G_f/H_i$ as a function of $2x^G_f/L_i$ and the dashed line is $2y^G_f/H_i = (8/9)(L_i/2x^G_f)$, which is the position of the mass center of any triangle having a surface $H_i L_i$.

Figure 14 shows the dimensionless vertical position $(2y^G - H_i)/H_i$ of the center of mass as a function of its horizontal position $(2x^G - L_i)/L_i$ for regime FF (black symbols), regime I (blue symbols), regime VI (red symbols), and regime V (brown symbols). In this figure, symbols correspond to the final state of the mass position $((2x^G_f - L_i)/L_i, (2y^G_f - H_i)/H_i)$. For comparison, the evolution of the position of the center of mass $((2x^G - L_i)/L_i, (2y^G - H_i)/H_i)$ during the collapse is also shown for a few runs in the different regimes (dashed lines). At this scale of observation, all results match on the same leading curve. This means that, at least at leading order, the center of mass of the granular media follows a universal curve, the only difference between the different aspect ratios and flow regimes being its final position on this curve. These general observations emphasize the geophysical parametrization discussed in the preceding section, accounting for a simple process of fluid dissipation on the granular collapse. Once again, depending on the expected accuracy of the model, such an assumption could hold.

The inset of Fig. 14 shows $2y^G/H_i$ as a function of $2x^G/L_i$ and the dashed line corresponds to $2y^G_f/H_i = (8/9)(L_i/2x^G_f)$, which is the position of the center of mass of any triangle having a surface $H_i L_i$. As observed here, this simple geometry leads to a good prediction of the final shape of the deposit. One can observe that, at large $2x^G/L_i$, corresponding to increasing a and/or St, the solution deviates from the experimental results. This discrepancy can be associated with the curvature of the deposit, as observed in Fig. 13(a), for instance. We can note that, as the bottom plane is a smooth wall, the curvature of these profiles is slightly intensified at large St. However, whatever the roughness imposed at the bottom, such concavity is always obtained [7,10]. We therefore assert that the present observation is representative of any collapse in a liquid, even if a modification of the roughness would probably slightly modify the obtained curvature. This curvature could therefore be mostly attributed to inertia on the dynamics of the collapse which tends to disappear when St vanishes. In the latter case, the dynamics can be assumed to be quasistatic. The final constant slope obtained is therefore close to an angle of equilibrium of the granular material and this will be discussed in Sec. V B. For now, we propose a deeper investigation of the slope angle as a function of St.

As the shape of the final deposit can be more or less curved, we propose here to define two angles to characterize it. In particular, one defines an angle α_s close to the summit, i.e., at $x = x_c$, and an angle α_f at the foot, i.e., at $x = L_f$, of the final deposit (see Fig. 12). These two local angles, i.e.,
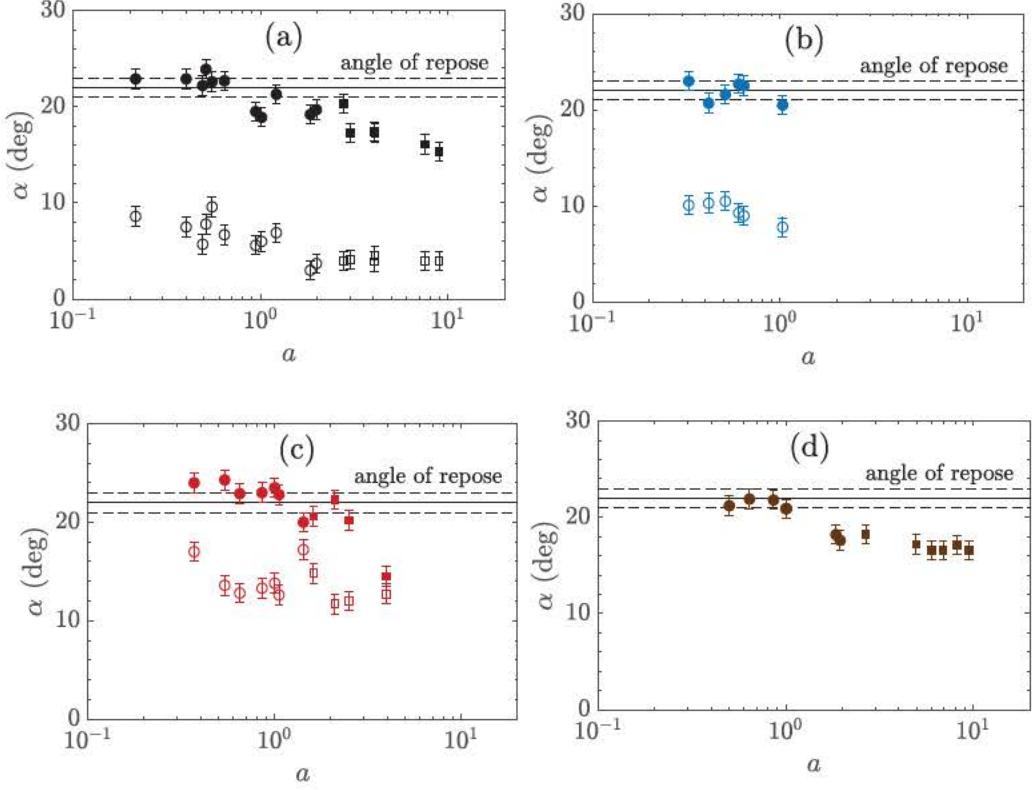
FIG. 15. Local angles α_s at the summit (closed symbols) and α_f at the foot (open symbols) as a function of the aspect ratio a for (a) regime FF, (b) regime I, (c) regime VI, and (d) regime V.

α_s (closed symbols) and α_f (open symbols), are shown in Fig. 15 as a function of a for regime FF [Fig. 15(a)], regime I [Fig. 15(b)], regime VI [Fig. 15(c)], and regime V [Fig. 15(d)]. As in Fig. 13, only deposits with smooth shape are considered here, the analysis of other inertial cases being postponed to Sec. V C. As expected, $\alpha_f < \alpha_s$ except for regime V, in which $\alpha_f = \alpha_s$. Also, the discrepancy $\alpha_s - \alpha_f$ increases with the Stokes number. One first observes that α_s is almost constant at small a with a value which is comparable to the angle of repose of the granular material (solid lines). When the aspect ratio a increases, the angle α_s suddenly decreases above $a \sim 1$ for all the regimes (when available) and eventually saturates to a slightly smaller value. This decrease, even if quite small [only 3° in Fig. 15(d)], is above the measurement accuracy and it is systematically observed. This observation is not explained here, but it seems to be correlated to the transition from trapezoidal to triangular deposit shape, when the point x_c (see Fig. 12) reaches the back wall of the reservoir. Note, on the other hand, that α_f decreases at small a until it reaches a constant value with the same transition $a \sim 1$. However, the a dependence of α_s and α_f remains small compared to the difference between these two angles as well as the evolution of α_f with St.

The average values $\langle \alpha_s \rangle$ and $\langle \alpha_f \rangle$ over a is reported in Fig. 16 as a function of St. One observes, as previously mentioned, that $\langle \alpha_s \rangle$ is roughly constant and about equal to the angle of repose of the granular material, i.e., $\langle \alpha_s \rangle \sim \alpha_r$ (solid lines in Fig. 16). On the other hand, $\langle \alpha_f \rangle$ decreases with the increase of St quantifying the curvature of the deposit shape profiles. At large St, the lower value of $\langle \alpha_f \rangle$ illustrates the stretching of the deposit due to the inertia flow. At low St, $\langle \alpha_f \rangle$ tends towards $\langle \alpha_s \rangle$ and then $\langle \alpha_s \rangle \sim \langle \alpha_f \rangle \sim \alpha_r$. This means that inertia becomes negligible and that the system evolves in a quasistatic state towards its final deposit with a constant angle equal to about the angle of repose.
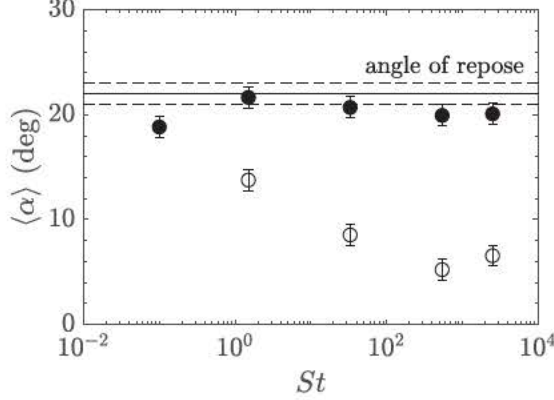
FIG. 16. Average values $\langle \alpha_f \rangle$ (open symbols) and $\langle \alpha_s \rangle$ (closed symbols) as a function of St.

B. Predictive model for the final deposit

In the preceding section, we show that the granular material tends towards its final deposit with a quasistatic state for decreasing St. This corresponds to a constant final slope of the deposit close to the angle of repose α_r. Combining this result with a final deposit described with a trapezoidal or a triangular shape as a function of a, one can therefore obtain a simple prediction of the final runout length and final height in the St $\to 0$ limit [7]. For this purpose, one assumes that the angle of repose α_r is associated with a constant coefficient of friction μ_d as $\mu_d = \tan \alpha_r$. Based on the mass conservation between the initial and the final states, one can show that the trapezoid and the triangle lead to the following scalings, respectively:

$$\frac{L_f - L_i}{L_i} = \frac{a}{2\mu_d}, \quad \frac{H_f}{L_i} = a, \tag{10}$$

$$\frac{L_f}{L_i} = \sqrt{\frac{2a}{\mu_d}}, \quad \frac{H_f}{L_i} = \sqrt{2a\mu_d}. \tag{11}$$

These two solutions explain the scaling laws obtained for the granular collapse and are presented in Sec. III. In particular, the linear dependence of $(L_f - L_i)/L_i$ with a in the solution (10) is consistent with results obtained at small a shown in Fig. 4(a) at which the trapezoidal shape is more likely to be observed. On the other hand, the solution (11) obtained for a triangle is usually observed at larger a. This scaling law is indeed consistent with results obtained in the inset of Fig. 4(a). As observed in the inset of Fig. 4(a), the triangular scaling with $L_f/L_i \sim a^{1/2}$ is shown to be pertinent on a larger range of a, which makes it more pertinent for the range of parameters considered here. We then focus on this specific shape in the following.

Once inertia is not negligible, for St $\gg 1$, the curvature of the final deposit is more pronounced. If one assumes that the slope of the deposit is not constant anymore but that the height profile $h(x)$ can be defined as a second-order polynomial in x for the final deposit, with a fixed angle at $x = 0$ equal to the angle of repose (see $\langle \alpha_s \rangle$ in Fig. 16), then one obtains $h(x) = (\mu_d - H_f/L_f)\frac{x^2}{L_f} - \mu_d x + H_f$. Assuming that the slope at the foot, i.e., at $x = L_f$, is associated with a coefficient of friction $\mu_{St} = \tan \alpha_f$ which decreases with increasing St (see $\langle \alpha_f \rangle$ in Fig. 16), one obtains for the triangle the scaling

$$\frac{L_f}{L_i} = \sqrt{\frac{6a}{\mu_d + 2\mu_{St}}}, \quad \frac{H_f}{L_i} = \sqrt{\frac{3a(\mu_d + \mu_{St})^2}{2(\mu_d + 2\mu_{St})}}, \tag{12}$$
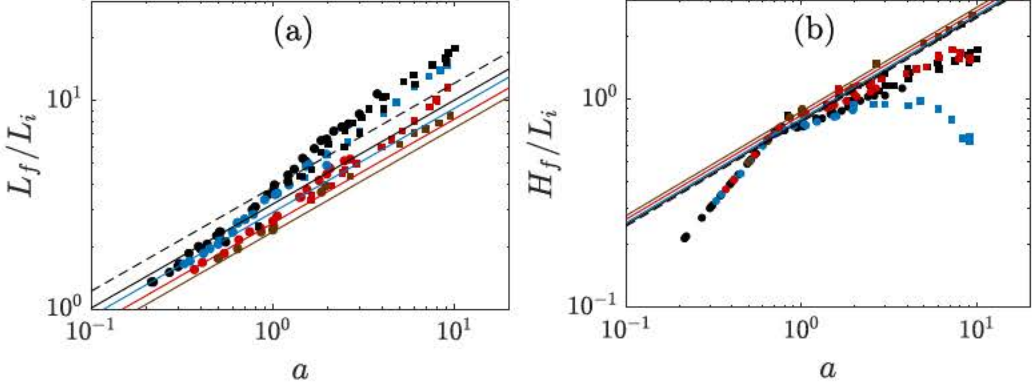
FIG. 17. (a) Dimensionless runout length L_f/L_i and (b) final height H_f/L_i as a function of the aspect ratio $a = H_i/L_i$ for regime FF (black), regime I (blue), regime VI (red), and regime V (brown). Symbols are experiments and lines are predictive models (12) (solid lines) and (13) (dashed lines). In the latter cases, $\mu_d = \tan\alpha_r$, where $\alpha_r = 22\mathrm{o}$ is the angle of repose, and $\mu_{St} = \tan\langle\alpha_f\rangle$, where $\langle\alpha_f\rangle$ is the mean angle at the foot of the deposit and determined from Fig. 16.

which becomes in the asymptotic limit $\mu_{St} \to 0$ when $St \to \infty$,

$$\frac{L_f}{L_i} = \sqrt{\frac{6a}{\mu_d}}, \quad \frac{H_f}{L_i} = \sqrt{\frac{3a\mu_d}{2}}. \tag{13}$$

The predictive models (12) and (13) are compared to experimental results in Fig. 17. In particular, the dimensionless runout length L_f/L_i [Fig. 17(a)] and the final height H_f/H_i [Fig. 17(b)] are plotted as a function of the aspect ratio a for regime FF (black symbols), regime I (blue symbols), regime VI (red symbols), and regime V (brown symbols). Experiments are represented with symbols while the predictive models (12) and (13) correspond to solid lines and dashed lines, respectively. It can be first noted that the model predicts a longer runout length at large St than otherwise. Also, the predicted discrepancy has the same order of magnitude as for experimental results. However, at large a, this model underestimates (overestimates) the runout length L_f/L_i (the final height H_f/L_i), which can be attributed to the simplicity of the description of the height profile with a second-order polynomial in the triangle case. Surprisingly, we can note that, at low a, the runout length L_f/L_i is well predicted by the proposed model, yet the latter does not consider the trapezoidal shape of the final deposit.

C. Final morphology in the fluid inertial regime

In the previous sections, the final deposit for regimes I and VI at large a was disregarded. The reason for that was the observation of a spatial oscillation, a bump, of the final deposit surface, which appears above $a \sim 1$ and 4, respectively. This specific deposit shape has already been observed in the dry case, as well for initially fluidized granular flows [20,31] as for granular collapses [14,15,17,26]. The spatial structure makes the analysis more complex and some of the arguments used previously are not valid. Note that this feature is another signature of the fluid inertia on the granular flow dynamic as it is mostly observed in regime I for a large enough, i.e., for $(d/H_i)^{1/2}r_c \ll 1$ (see Fig. 10). In this case, a decrease of the final height H_f/L_i with increasing a is then observed, while it is usually increasing for other regimes [see Fig. 4(b)]. This trend appears to be linked to the appearance of a surface bump close to the collapse front, most of the mass being transferred from the back wall $x = 0$ to a location closer to the front position (see the final deposit in the inertial regime with $a = 9$, Fig. 3, and the movie in the Supplemental Material [28]). We then briefly describe the shape of this observed surface bump in the following. For this purpose, as the final deposit mostly highlights a
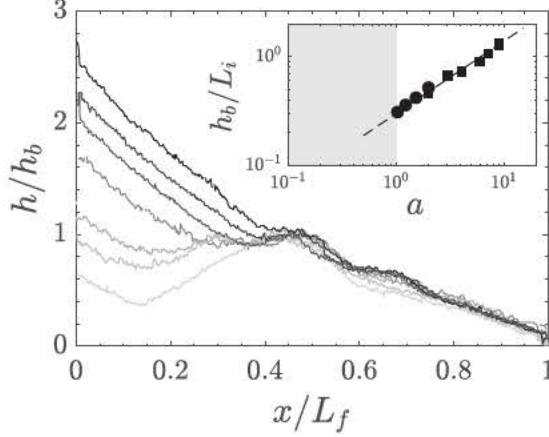
FIG. 18. Height profile h/h_b as a function of x/L_f for regime I. The aspect ratio is in the range $a = [1,9]$ (from black to light gray, respectively). The inset shows h_b/L_i as a function of a. No bump is observed in the gray area.

local maximum at $x > 0$ in this case, the final deposit is thus characterized, among previous scalings, by the final height h_b of this local maximum at $x_b > 0$.

Figure 18 shows the dimensionless height profile h/h_b as a function of x/L_f for regime I. The aspect ratio is in the range $a = [1,9]$ (from black to light gray, respectively). For $0 < x/L_f < 0.5$, it can be noted that h/h_b decreases for increasing a. On the other hand, for $0.5 < x/L_f < 1$, the dimensionless height profile is similar to whatever the value of a is in the range of parameters considered here. This latter observation is similar to the similarity of the height profiles mentioned in the preceding section, but now only holds for the region in front of the bump. These observations clearly reveal that for increasing aspect ratio, the mass is transferred from the back wall, at $x = 0$, to the front position, at $x = L_f$. Moreover, the shape similarity property of the final deposit described in previous sections for simpler deposits is shown to hold close to the front for more complex deposits. The inset of Fig. 18 shows the evolution of h_b/L_i as a function of a. For $a < 1$, i.e., the gray area, no bump is observed on the final deposit. Above this value, the dimensionless height h_b/L_i increases with a. Note that this corresponds to the range of a in which H_f/L_i was shown to decrease with increasing a [see Fig. 4(b)]. We find here that this evolution of h_b with a follows a simple power law $h_b/L_i \sim a^{2/3}$.

VI. CONCLUSION

Laboratory experiments on the collapse of a dense granular column in a fluid have been investigated. In particular, the viscosity and the density of the surrounding fluid were varied. Both the dynamics of the granular flow and the final deposit of the granular medium have been characterized due to the temporal evolution of the granular height profiles. More specifically, this present study focused on the influence of the Stokes number St, the grain-fluid density ratio r, and the aspect ratio a of the initial granular column. First, it was shown that the runout length L_f and the final height H_f of the final deposit are mainly controlled by a and St. The runout length is restricted to an interval limited by the dry regime and the viscous regime. With appropriate scaling, it follows simple power laws with a, i.e., $(L_f - L_i)/L_i = \lambda_1 a$ for $a \lesssim 2$ and $(L_f - L_i)/L_i \sim \lambda_2 a^{0.64}$ for $a \gtrsim 2$, while St modifies only the prefactors λ_1 and λ_2. Also, the final height has a power-law dependence on a except for the inertial regime, at large a, where the final deposit shape is more complex. It was shown that this observed modification of the final height scaling laws for a fluid inertial regime is associated with the appearance of a surface bump transferring mass from the back wall $x = 0$ towards the

collapse front. This dimensionless bump height has been shown to be a power law of a similar to the one obtained for H_f/L_i when no surface bump is observed. Furthermore, the collapse dynamics of the granular column is strongly affected by the surrounding fluid. Initially, a trigger time, i.e., an expansion time that the dense granular medium needs to flow, was observed which increases with decreasing St. Following this initial stage, the granular column collapses with a characteristic time dependent on the regime considered. More specifically, a map of granular flow regimes (free-fall, inertial, and viscous) was proposed in the $((d/H_i)^{1/2}\text{St},(d/H_i)^{1/2}r)$ plane defined herein. Moreover, a simple correlation of the maximum velocity of the collapse with the classical free-fall velocity, involving dissipation through the Stokes number, was provided. Finally, a deep investigation of the characterization of the deposit morphology was proposed. The temporal evolution of the position of the center of mass was shown to follow a universal curve and only its final state is affected by the considered regime and the aspect ratio. Then, as a result of the concave shape of the deposit, two angles, at the summit and at the foot of the avalanche slope, were defined. The first angle is close to the angle of repose of the granular material, while the second angle depends strongly on the Stokes number. Considering this St dependence, a simple predictive model for a triangular deposit was proposed in the interest of geophysical applications.

APPENDIX: COMPARISON TO THE EXPERIMENT OF REF. [7]

In a previous study on the immersed granular collapse, Rondon *et al.* [7] studied the role of (ϕ,a) in the viscous regime, for $(\text{St},r) \sim (0.03–0.07,1.6)$. This appendix aims to compare their results with the present study in order to discuss the relative influence of ϕ (from [7]) and St (present study) on the granular collapse configuration. In particular, this comparison is based on the characteristics of the final shape deposit, which are the runout length and the final height. Figure 19 shows the normalized runout length L_f/L_i [Fig. 19(a)] and the final height H_f/H_i [Fig. 19(b)] as a function of the aspect ratio a. Pluses correspond to experiments performed in the present study for regime FF with $(\text{St},r,\phi) = (540–2500,43–46,0.64)$ (black) and regime V with $(\text{St},r,\phi) = (0.1,1.5,0.64)$
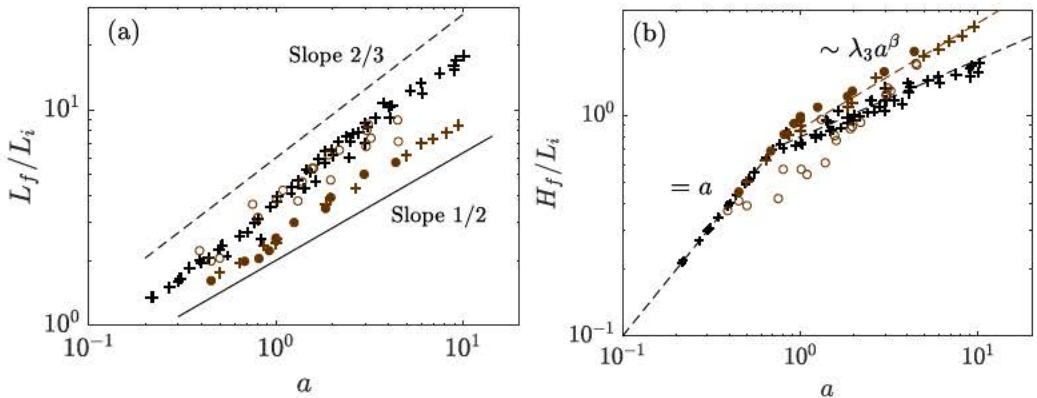

FIG. 19. (a) Dimensionless runout length L_f/L_i and (b) final height H_f/L_i as a function of the aspect ratio $a = H_i/L_i$. Pluses correspond to experiments performed in the present study, with $\phi \sim 0.64$, for regime FF (black) and regime V (brown), while circles are extracted from Ref. [7] with $\phi = 0.60$ (closed) and $\phi = 0.55$ (open) in the case of a granular collapse immersed in a viscous fluid.

(brown), while brown circles are extracted from [7] with $(St, r, \phi) = (0.03–0.07, 1.6, 0.6)$ (closed) and $(St, r, \phi) = (0.03–0.07, 1.6, 0.55)$ (open). It can be first noted that for similar ϕ, St, and r, i.e., $(St, r, \phi) = (0.1, 1.5, 0.64)$ in our study (brown pluses) and $(St, r, \phi) = (0.03–0.07, 1.6, 0.6)$ in [7] (brown closed circles), results are in very good agreement for both the final spreading length and final height. This observation supports again the pertinence of the dimensionless numbers used, as different fluid-grain properties were used by Rondon *et al.* [7]. Moreover, it can observed that for decreasing ϕ (from closed to open circles) or for increasing St (from brown to black pluses), the dimensionless runout length L_f/L_i increases (the dimensionless final height H_f/L_i decreases). In both cases, this can be attributed to the influence of the ambient fluid on the dynamics of the granular medium, leading to a decrease of viscous dissipation when St increases or a modification of the pore pressure when ϕ decreases [7]. These two phenomena are somehow linked as the inward fluid flow induced by a negative pore pressure when ϕ is about the random close packing tends to disappear when ϕ decreases. The viscous dissipation due to this inward flow on the granular dynamics then only exists when the granular motion implies a decompaction of the medium, i.e., when ϕ is close to the close packing, and is only significant when the fluid properties are such that viscous effects are important, i.e., at small St. This is probably the reason why the two cases, large St and small ϕ, compare well for the runout length in Fig. 19(a), even if some other processes differ from the two situations.

[1] Y. Forterre and O. Pouliquen, Flows of dense granular media, Annu. Rev. Fluid Mech. **40**, 1 (2008).
[2] R. Delannay, A. Valance, A. Mangeney, O. Roche, and P. Richard, Granular and particle-laden flows: From laboratory experiments to field observations, J. Phys. D **50**, 053001 (2017).
[3] S. Courrech du Pont, P. Gondret, B. Perrin, and M. Rabaud, Granular Avalanches in Fluids, Phys. Rev. Lett. **90**, 044301 (2003).
[4] C. Cassar, M. Nicolas, and O. Pouliquen, Submarine granular flows down inclined planes, Phys. Fluids **17**, 103301 (2005).
[5] E. L. Thompson and H. E. Huppert, Granular column collapses: Further experimental results, J. Fluid Mech. **575**, 177 (2007).
[6] M. Pailha, M. Nicolas, and O. Pouliquen, Initiation of underwater granular avalanches: Influence of the initial volume fraction, Phys. Fluids **20**, 111701 (2008).
[7] L. Rondon, O. Pouliquen, and P. Aussillous, Granular collapse in a fluid: Role of the initial volume fraction, Phys. Fluids **23**, 073301 (2011).
[8] V. Topin, Y. Monerie, F. Perales, and F. Radjaï, Collapse Dynamics and Runout of Dense Granular Materials in a Fluid, Phys. Rev. Lett. **109**, 188001 (2012).
[9] G. Lube, H. E. Huppert, R. S. J. Sparks, and M. A. Hallworth, Axisymmetric collapses of granular columns, J. Fluid Mech. **508**, 175 (2004).
[10] E. Lajeunesse, A. Mangeney-Castelnau, and J. P. Vilotte, Spreading of a granular mass on a horizontal plane, Phys. Fluids **16**, 2371 (2004).
[11] G. Lube, H. E. Huppert, R. S. J. Sparks, and A. Freundt, Collapses of two-dimensional granular columns, Phys. Rev. E **72**, 041301 (2005).
[12] N. J. Balmforth and R. R. Kerswell, Granular collapse in two dimensions, J. Fluid Mech. **538**, 399 (2005).
[13] E. Lajeunesse, J. B. Monnier, and G. M. Homsy, Granular slumping on a horizontal surface, Phys. Fluids **17**, 103302 (2005).
[14] L. Staron and E. J. Hinch, Study of the collapse of granular columns using two-dimensional discrete-grain simulation, J. Fluid Mech. **545**, 1 (2005).
[15] E. Larrieu, L. Staron, and E. J. Hinch, Raining into shallow water as a description of the collapse of a column of grains, J. Fluid Mech. **554**, 259 (2006).

[16] C. Mériaux, Two dimensional fall of granular columns controlled by slow horizontal withdrawal of a retaining wall, Phys. Fluids **18**, 093301 (2006).

[17] L. Staron and E. J. Hinch, The spreading of a granular mass: Role of grain properties and initial conditions, Granular Matter **9**, 205 (2007).

[18] L. Lacaze, J. C. Phillips, and R. R. Kerswell, Planar collapse of a granular column: Experiments and discrete element simulations, Phys. Fluids **20**, 063302 (2008).

[19] C. Meruane, A. Tamburrino, and O. Roche, On the role of the ambient fluid on gravitational granular flow dynamics, J. Fluid Mech. **648**, 381 (2010).

[20] O. Roche, M. Attali, A. Mangeney, and A. Lucas, On the run-out distance of geophysical gravitational flows: Insight from fluidized granular collapse experiments, Earth Planet. Sci. Lett. **311**, 375 (2011).

[21] A. Daerr and S. Douady, Sensitivity of granular surface flows to preparation, Europhys. Lett. **47**, 324 (1999).

[22] R. M. Iverson, M. E. Reid, N. R. Iverson, R. G. LaHusen, M. Logan, J. E. Mann, and D. L. Brien, Acute sensitivity of landslide rates to initial soil porosity, Science **290**, 513 (2000).

[23] O. Roche, S. Montserrat, Y. Nino, and A. Tamburrino, Experimental observations of water-like behavior of initially fluidized, dam break granular flows and their relevance for the propagation of ash-rich pyroclastic flows, J. Geophys. Res. Solid Earth **113**, B12203 (2008).

[24] R. R. Kerswell, Dam break with Coulomb friction: A model for granular slumping? Phys. Fluids **17**, 057101 (2005).

[25] L. Lacaze and R. R. Kerswell, Axisymmetric Granular Collapse: A Transient 3D Flow Test of Viscoplasticity, Phys. Rev. Lett. **102**, 108305 (2009).

[26] P.-Y. Lagrée, L. Staron, and S. Popinet, The granular column collapse as a continuum: Validity of a two-dimensional Navier-Stokes model with a $\mu(I)$-rheology, J. Fluid Mech. **686**, 378 (2011).

[27] K. Kumar, J.-Y. Delenne, and K. Soga, Mechanics of granular column collapse in fluid at varying slope angles, J. Hydrodyn. **29**, 529 (2017).

[28] See Supplemental Material at http://link.aps.org/supplemental/10.1103/PhysRevFluids.3.064305 corresponding to granular collapses, for regime FF, regime V, and regime I with $a = 1$ and for regime I with $a = 9$.

[29] H. E. Huppert and J. E. Simpson, The slumping of gravity currents, J. Fluid Mech. **99**, 785 (1980).

[30] I. M. Jánosi, J. Dominique, K. G. Szabó, and T. Tél, Turbulent drag reduction in dam-break flows, Exp. Fluids **37**, 219 (2004).

[31] O. Roche, M. A. Gilbertson, J. C. Phillips, and R. S. J. Sparks, Experimental study of gas-fluidized granular flows with implications for pyroclastic flow emplacement, J. Geophys. Res. **109**, B10201 (2004).

[32] R. Turton and O. Levenspiel, A short note on the drag correlation for spheres, Powder Technol. **47**, 83 (1986).

[33] J. Rottman and J. Simpson, Gravity currents produced by instantaneous releases of a heavy fluid in a rectangular channel, J. Fluid Mech. **135**, 95 (1983).